

1 **The impact of turbulence on flying insects**
2 **in tethered and free flight:**
3 **high-resolution numerical experiments**

4 Thomas Engels*

5 *LMD-CNRS, École Normale Supérieure and PSL, Paris, 24 rue Lhomond, 75231 Paris Cedex 05, France*

6 Dmitry Kolomenskiy

7 *Japan Agency for Marine-Earth Science and Technology (JAMSTEC),*
8 *3173-25 Showa-machi, Kanazawa-ku, Yokohama Kanagawa 236-0001, Japan.*

9 Kai Schneider

10 *Aix-Marseille Université, CNRS, Centrale Marseille, I2M UMR 7373,*
11 *Marseille, 39 rue Joliot-Curie, 13451 Marseille Cedex 20 France*

12 Marie Farge

13 *LMD-CNRS, Ecole Normale Supérieure and PSL, Paris, 24 rue Lhomond, 75231 Paris Cedex 05, France*

14 Fritz-Olaf Lehmann

15 *Department of Animal Physiology, Universität Rostock,*
16 *Rostock, Albert-Einstein-Str. 3, 18059 Rostock, Germany*

17 Jörn Sesterhenn

18 *ISTA, Technische Universität Berlin, Berlin, Müller-Breslau-Strasse 12, 10623 Berlin, Germany*

19 (Dated: 20 April 2018)

Flapping insects are remarkably agile fliers, adapted to a highly turbulent environment. We present a series of high resolution numerical simulations of a bumblebee interacting with turbulent inflow. We consider both tethered and free flight, the latter with all six degrees of freedom coupled to the Navier–Stokes equations. To this end we vary the characteristics of the turbulent inflow, either changing the turbulence intensity or the spectral distribution of turbulent kinetic energy. Active control is excluded in order to quantify the passive response real animals exhibit during their reaction time delay, before the wing beat can be adapted. Modifying the turbulence intensity shows no significant impact on the cycle-averaged aerodynamical forces, moments and power, compared to laminar inflow conditions. The fluctuations of aerodynamic observables, however, significantly grow with increasing turbulence intensity. Changing the integral scale of turbulent perturbations, while keeping the turbulence intensity fixed, shows that the fluctuation level of forces and moments is significantly reduced if the integral scale is smaller than the wing length. Our study shows that the scale-dependent energy distribution in the surrounding turbulent flow is a relevant factor conditioning how flying insects control their body orientation.

* thomas.engels@ens.fr

I. INTRODUCTION

Insect are fast and agile fliers, which stabilize their body posture during flight under a vast variety of environmental conditions [5, 37]. While flight in static air requires little steering and corrective changes in aerodynamic force production, flight in turbulent air is challenged by unexpected changes in flow conditions at the body and wings. Little is known about the impact of turbulence on the aerodynamic performance and energetic cost of flight in insects. In this work, we study how different kinds of perturbations affect flapping fliers in free flight.

In contrast to laminar flows, turbulent flows are dominated by nonlinear interactions and, as a result, excite fluctuations on a wide range of scales. After averaging the flow in either ensemble, time or space, we identify different length scales characteristic for the turbulent regime. From large to small, these classical scales are: (i) the integral scale Λ where, on average, the velocity is the strongest, and where therefore energy transport is most active, (ii) the Taylor microscale λ where, on average, the velocity gradients are most intense, (iii) the Kolomogorov scale η below which, on average, the flow fluctuations are damped by the fluid viscosity [47].

In nature, unsteady turbulent flow conditions significantly vary depending on the terrain and weather conditions. The “flight boundary layer”, characterized by conditions favorable for insect flight, can span for up to 1500 meters above the ground level in warm weather [6]. Activity such as long-distance migration is typical of high altitudes while foraging, for example, mainly takes place in the vegetation layer up to several meters above the ground. This diversity of flow conditions, besides variation in the temperature, density and mean wind speed, exposes flying insects to a variety of turbulent flows, ranging from those dominated by wakes and canopy-layer turbulence at low altitude [23, 48, 49], to the atmospheric turbulence determined by weather and wind systems at high altitude [59, 60].

Until now, studies have focused on selected model organisms such as hummingbirds [44], moths [27, 43], bumblebees [50, 51], etc., subject to archetypal air flow conditions such as von Kármán wakes [43, 50, 51] or grid turbulence [10]. In the hawkmoths *Manduca sexta*, for example, yaw and roll oscillations of the animal body are synchronized with the vortex shedding frequencies in the wake behind a large cylinder [43]. Vortex shedding in von Kármán wakes, however, differs from turbulence since, at moderate Reynolds numbers, vortices are shed periodically in time and the flow has strong spatial correlations. Few numerical [18] and experimental [10, 11] studies addressed flapping flight in turbulent flow and estimated flow conditions at body and wings. In heavy turbulence, for example, bumblebees are highly prone to changes in roll stability and crash if roll velocity exceeds a maximum value [10].

High maneuverability in flight is likely key in coping with turbulence, at the cost of low stability [26, 27]. Insects that stabilize their body posture during aerial perturbations thus require fast feedback responses. These responses may rely on passive and active changes of wing- and body kinematics. Both mechanisms might help to mitigate aerial perturbations. While passive changes of wing kinematics result from the interplay between wing material properties and inertial/aerodynamic forces and thus elastic wing deformation [9, 21, 34, 39, 40, 53] active control is imposed by the sensomotor system of the animal and thus changes in flight muscle activation [13]. A complex passive mechanism has been reported for the fruit fly *Drosophila* [2]. The latter study suggests that wing rotation about the wing’s longitudinal axis [34] behaves like a system composed of a damped torsion spring. The animal might control wing rotation by actively changing stiffness and damping coefficients of this spring, as well as the resting feathering angle. In this case, fluid–structure interaction results from a combination of passive changes *via* spring deformation and active changes *via* modifications of the spring’s elastic property.

Besides passive changes, insects also possess a large variety of active control mechanisms for body stabilization and flight heading control. Studies on flight control highlighted several unique mechanisms of wing motion modulation in insects (see [12] for a recent review). These mechanisms include changes in stroke amplitude, stroke frequency, stroke plane, the wing’s angle of attack and timing of wing rotation at the end of each half stroke [10, 24]. Freely flying bumblebees, for example, stabilize body roll by changes of the relative difference between left and right stroke amplitude [11]. Insects also actively change body shape that modifies their inertia tensor during flight. Fruit flies [3], hawkmoths [41] and chestnut tiger butterflies [61], for example, change and stabilize their flight heading by changing the angle between thorax and abdomen.

Previous studies considered the body roll axis of an animal to be most susceptible for aerodynamic perturbations, owing to its small moment of inertia compared to yaw and pitch. Flying through turbulence thus produces largest fluctuations about the roll axis in insects [50]. To minimize these changes, some insects laterally extend their hind legs that increases the roll moment of inertia [10]. Although this behavior has been found in orchid bees, smaller insects such as the fruit fly benefit only little from this mechanism owing to their small legs [3]. Since the hind legs of orchid bees are untypically large compared to other insect species, it is less likely that the latter mechanism represents a common mechanism for roll control in insect flight [3]. A most significant mechanism to cope with air turbulence is aerodynamic damping, resulting from the flapping wing motion. It is termed flapping-counter-torque [8, 26, 27] and primarily acts in the direction perpendicular to the stroke plane. In a horizontal stroke plane, roll damping only occurs if left and right wings flap at different angle of attack [22]. In an inclined stroke plane, the moment vector is deflected from the vertical and contributes to roll dynamics, even during symmetrical motion of both wings. The concept of flapping-counter-torque in insects was extended to damping coefficients for all six degrees of freedom of body motion [7].

To understand body posture control of insects flying in turbulent air, we here present a numerical study. Our study models

and compares flight of both a tethered and freely flying insect (bumblebee). We consider different turbulent flows and vary their turbulence intensity as well as their characteristic length scales, *e.g.*, the integral scale. Under free flight conditions, the model insect is allowed to translate along and rotate about all three body axes, in response to aerodynamic, inertial and gravitational forces, and moments, respectively. However, we exclude any active control in this work.

Our previous study [18] showed that in tethered flight even strong inflow turbulence has little effect on mean force production and moments, and thus on aerodynamic mechanisms. Building on this finding, we here explore the effects of turbulent length scales on a freely flying insect model and demonstrate the effect of turbulence on body posture in free flight. The approach allows body motion but ignores any *passive* deformation, of both body and wing, and also *active* steering. Our study investigates if and how the scale-dependent energy distribution is relevant for body orientation control in flying insect.

The complicated time-dependent geometry and the resulting complex flow topology challenge numerical simulations of insect flight. There are two major numerical approaches for this problem. (i) Overset grids [35, 36, 55], which allow strong refinement near surfaces, but considering inflow turbulence is practically excluded because of difficulties in parallelization and hence limited resolution. (ii) Immersed Boundary Methods (IBM) which disconnect the flapping motion from the grid and thus simplifies the discretization. For flapping flight, finite volume [32, 38] or lattice-Boltzmann type simulations [28, 56] are successful numerical methods combined with IBM. Here, we use the volume penalization method combined with a Fourier pseudospectral solver [20]. This numerical method is characterized by the absence of numerical dissipation, its high efficiency on massively parallel computers thanks to the optimized implementation of FFTs [45] and the possibility to impose turbulent inflow.

The remainder of the manuscript is organized as follows: the computational setup is illustrated in section II A and the characteristics of inflow turbulence are described in section II B. Section II C presents the bumblebee model and section II D recalls the governing equations and briefly outlines the numerical method. The results and discussion section III presents first tethered flight simulations and then different free flight cases. Finally, conclusions are drawn in section IV and some possible directions for future work are proposed.

II. FLOW CONFIGURATION AND NUMERICAL METHOD

A. Numerical wind tunnel

We illustrate the computational set up and the flow configuration in Fig. 1. Simulations are performed in a $6R \times 4R \times 4R$ large virtual wind tunnel (Fig. 1A), where R is the wing length of the insect (see section II C). We initially place the insect at $\underline{x}_{\text{ctr}} = (2R, 2R, 2R)^T$ and either allow it to move freely as dictated by the fluid forces or tether it to that position. The resolution in space is $1152 \times 768 \times 768$ equidistant grid points, thus the lattice spacing is $\Delta = 5.2 \cdot 10^{-3}R$. The mean flow velocity is set to $\underline{u}_\infty = (1.246Rf, 0, 0)^T$, where f is the wing beat frequency. It compensates for the cruising speed of the insect in laminar flow. We initialize the simulation with unperturbed, laminar flow, $\underline{u}(\underline{x}, t = 0) = \underline{u}_\infty$. At the outlet, a vorticity sponge [19] minimizes the upstream influence of the periodicity of the computational domain. In the inlet region, which covers the first 48 grid points, the velocity is set to $\underline{u}_s = \underline{u}_\infty + \underline{u}'$, where \underline{u}' are velocity fluctuations obtained from a precomputed, homogeneous isotropic turbulence (HIT) velocity field (Fig. 1B). The properties of this field are discussed in section II B.

We rescale the HIT velocity field to insect dimensions preserving dynamic similarity, as HIT simulations are typically performed in a dimensionless manner. The field is then upsampled using zero-padding in Fourier space to match the resolution of the numerical wind tunnel (Fig. 1C). Note that the resolution requirement for the bumblebee is larger than for the HIT simulations in all considered cases, as required by the detailed geometry of the bumblebee. In cases with larger integral scale, we compute four identical bumblebees in one simulation with doubled lateral domain size and the same resolution (Fig. 1D), for reasons explained below.

Fig. 2 shows an example computation. Inside the inlet layer, the HIT field is frozen, *i.e.*, not dynamically evolving. Further downstream the turbulent flow evolves dynamically, and decays similar to what is observed in grid turbulence. The imposed constant mean flow u_∞ transports the turbulent/laminar interface, as illustrated in Fig. 2. It reaches the insect's head at $t/T = 0.95$ and its tail at $t/T = 1.95$. Thus all wing beats after the second one take place in turbulence and are used to compute the statistics. After $t/T = 3.21$, the periodic HIT field repeats, owing to the spatial periodicity of the precomputed field. For each statistical state of inflow turbulence, we compute a number of realizations N_R to be able to perform ensemble averaging. All simulations are identical except for the turbulent inflow field. For more technical details, we refer to [18, suppl. mat.].

B. Inflow turbulence

Flying animals encounter a considerable variety of aerial perturbations while foraging, ranging from no perturbation in almost quiescent air when the weather is calm, to fully turbulent, with intermittent gusts and vortices generated by obstacles, such as flowers, trees or buildings. The type of perturbation also depends on behavioral patterns in animals. Bees, for example, forage on flowers and thus regularly perform landing maneuvers which force them to fly in the flower's wake. Owing to this

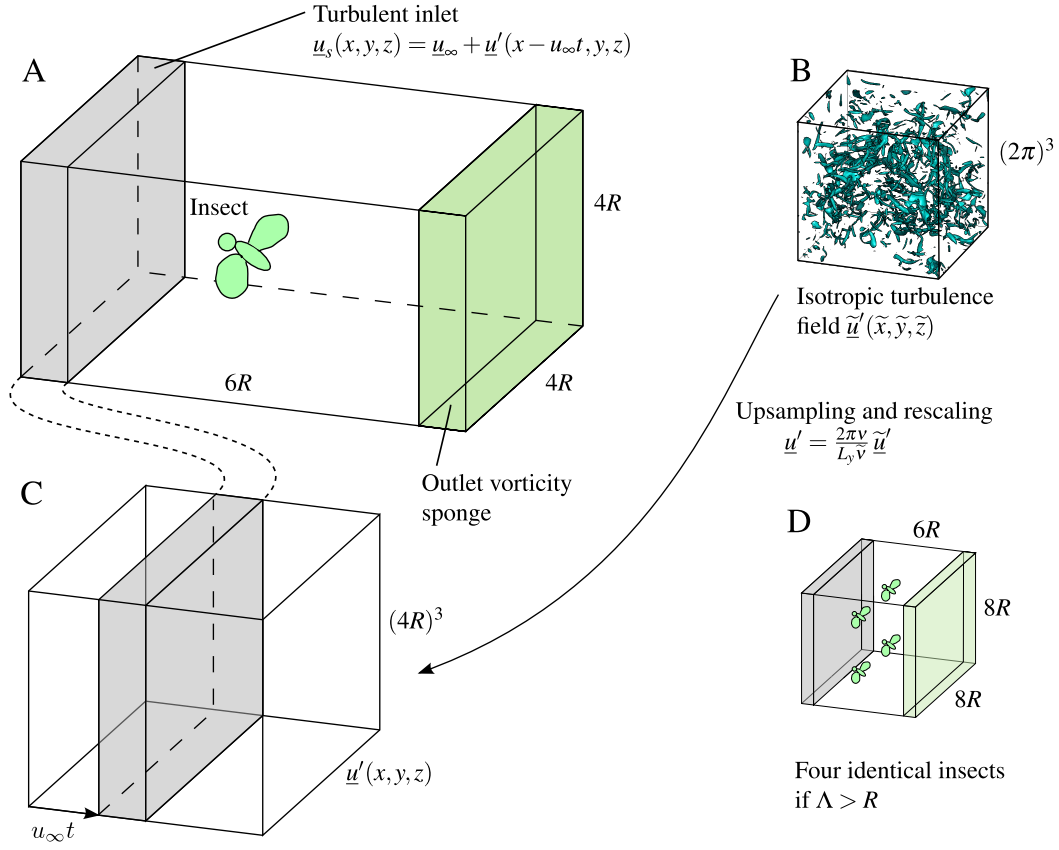


Figure 1. Setup used in present work. (A) Numerical wind tunnel, with tethered or freely flying insect. Turbulent inflow is imposed in the upstream gray area, a vorticity sponge in the downstream green area damps vortices and thus minimizes their upstream influence. The turbulent inlet imposes a slice of an isotropic turbulence field (B), which has been pre-computed in a separate simulation. The turbulence field has been upsampled (C) to match the resolution of the numerical wind tunnel and rescaled preserving dynamic similarity. The gray slice in (C) moves through the periodic field $u'(x, y, z)$ at constant speed u_∞ . In some simulations with larger integral scale Λ , four identical insects are computed (D) in one simulation, as explained in section II B.

huge variability in turbulent perturbations, we first reduce the parameter space. Therefore we define a typical turbulent flow and choose homogeneous isotropic turbulence (HIT) for the upstream perturbations because it is the most widely used. It is also realized in experimental work, e.g., generated by a grid in a wind tunnel [11]. HIT is characterized by its turbulent kinetic energy $E = 3u_{\text{RMS}}^2/2$, or equivalently the turbulence intensity $Tu = u_{\text{RMS}}/u_\infty$, the Reynolds number $Re_\lambda = u_{\text{RMS}}\lambda/\nu$, based on the Taylor-micro scale $\lambda = \sqrt{15\nu u_{\text{RMS}}/\varepsilon}$, and the integral length scale

$$\Lambda = \frac{\pi}{2u_{\text{RMS}}^2} \int_{k>0}^{\infty} k^{-1} E(k) dk.$$

Here, ν is the kinematic viscosity, ε the dissipation rate, k the wavenumber and $E(k)$ is the energy spectrum integrated over wavenumber shells. Note that for spatially periodic velocity fields, the integral reduces to a sum, as only integer wavenumbers $k \in \mathbb{N}$ exist. We pre-compute the HIT velocity fields in a separate direct numerical simulation. In this computation, energy is injected at a given wavenumber k_f to compensate for the loss due to viscous dissipation. Forced wavenumbers in the shell $k_f - 0.5 \leq |k| \leq k_f + 2.5$ are multiplied with a factor $c(t)$ to keep the overall energy constant in time. This approach is known as negative viscosity forcing [30, 31]. In all HIT computations, we resolve the Kolmogorov scale $\eta = (\nu^3/\varepsilon)^{1/4}$, hence $k_{\text{max}}\eta \gtrsim 1$. We start the HIT simulations with a random initial condition with prescribed spectrum [52]. After the statistically steady state has been reached, we save velocity fields for later use as inflow perturbations. The saving interval is at least 10 eddy turnover times to assure that the fields are uncorrelated in time. By modifying k_f at constant E and ν , we vary the spectral distribution of energy.

We generate two series of HIT simulations with turbulent kinetic energy spectra shown in Fig. 3. In series A we vary the intensity Tu from mildly ($Tu = 0.16$) to extremely ($Tu = 0.99$) turbulent while keeping the integral length scale $\Lambda = 0.77R$ fixed (Fig. 3 left). In series B where we fix $Tu = 0.33$ and vary $\Lambda = \{0.32R, 0.77R, 1.54R\}$ (Fig. 3 right). Turbulence properties are

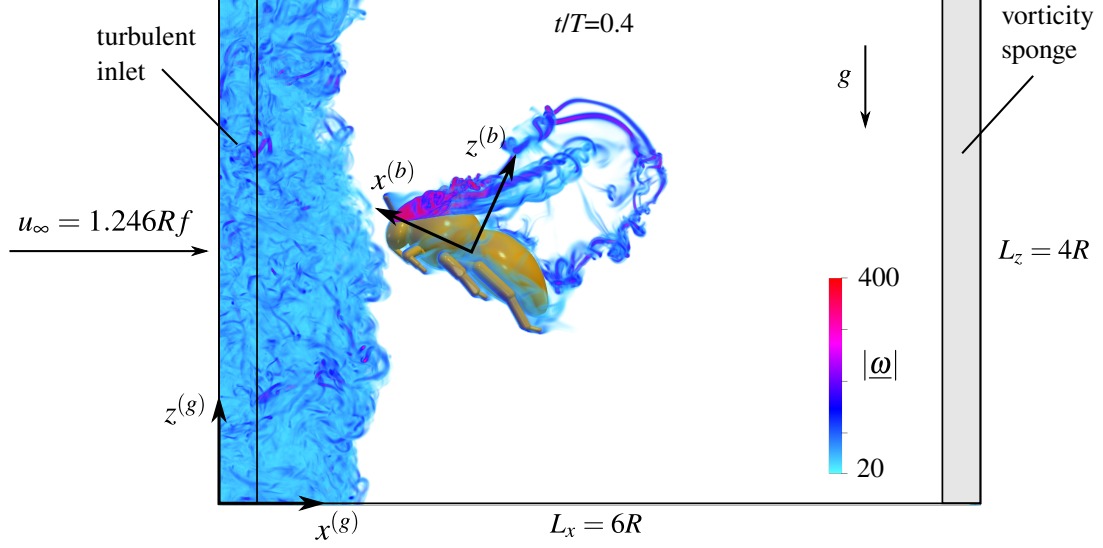


Figure 2. Snapshot of a simulation. The virtual bumblebee is tethered in the virtual wind tunnel, the mean flow u_∞ in $x^{(g)}$ direction compensates for the cruising speed of the insect. Reference frames shown are the global (g) and body-fixed (b). The flow field is visualized by the vorticity magnitude at an early instant ($t = 0.4T$) before the laminar/turbulent interface reaches the insect. The parameters are $Tu = 0.99$ and $\Lambda = 0.77R$.

Series	Tu	$\Lambda [R]$	$\lambda [R]$	$\eta [R]$	$T_0 [T]$	Re_λ	$k_{\max} \eta$	N_R	
								tethered	free
A	0.16	0.77	0.25	0.013	3.67	90	1.72	4	3
	0.33	0.77	0.18	0.008	0.19	129	1.07	5	16
	0.60	0.76	0.13	0.005	0.98	177	0.99	9	9
	0.99	0.76	0.11	0.004	0.62	227	0.94	27	6
B	0.33	1.54	0.26	0.01	3.62	186	1.32	10 ^(a)	–
	0.33	0.77	0.18	0.008	1.91	129	1.07	5	16
	0.33	0.32	0.11	0.006	0.77	82	1.70	5	15

(a) We computed two runs with four insects and an additional two runs with only one.

Table I. Properties of the homogeneous isotropic turbulence fields (time averaged over several eddy-turnover times) used as inflow perturbations for the insect. The rightmost column shows the number of realizations N_R used in tethered- and free flight simulations. Here, Tu is the turbulence intensity, which is equivalent to the turbulent kinetic energy, Λ is the integral scale, λ is the Taylor microscale, η the Kolmogorov scale and T_0 is the eddy turnover time. All quantities are given in units of wing length R and wing beat duration T .

summarized in Table I. The first series allows us to evaluate the impact of turbulence intensity, while the second series allows us to investigate the influence of Λ on the insect. Note that the eddy turnover time $T_0 = \Lambda/u'_{\text{RMS}}$ decreases, as expected, with increasing Tu (series A) and, likewise, with decreasing Λ (series B). We vary the energy distribution *via* the forcing wavenumber k_f in the HIT simulation. Note that in the $\Lambda = 0.77R$ case the forcing wavenumber was $k_f = 1$, thus we cannot reduce it any further in order to increase Λ . Therefore, in order to increase Λ to $1.54R$, we double the lateral domain size to $L_y = L_z = 8R$ in the insect simulation, which then allows $k_f = 1$ to result in a larger integral scale. With the larger domain, we then compute four identical insects in one simulation (Fig. 1D), to reduce the computational cost.

Fig. 4 illustrates two individual HIT fields from the B series by showing the isosurface of vorticity $|\omega| = 4\sigma(\omega)$, where σ is the corresponding standard deviation. The energy E of both fields is the same, but the integral scales are $\Lambda = 1.54R$ and $0.32R$, respectively. Visibly, the $\Lambda = 0.32R$ case features smaller scale vortices which are more densely distributed in the periodic box.

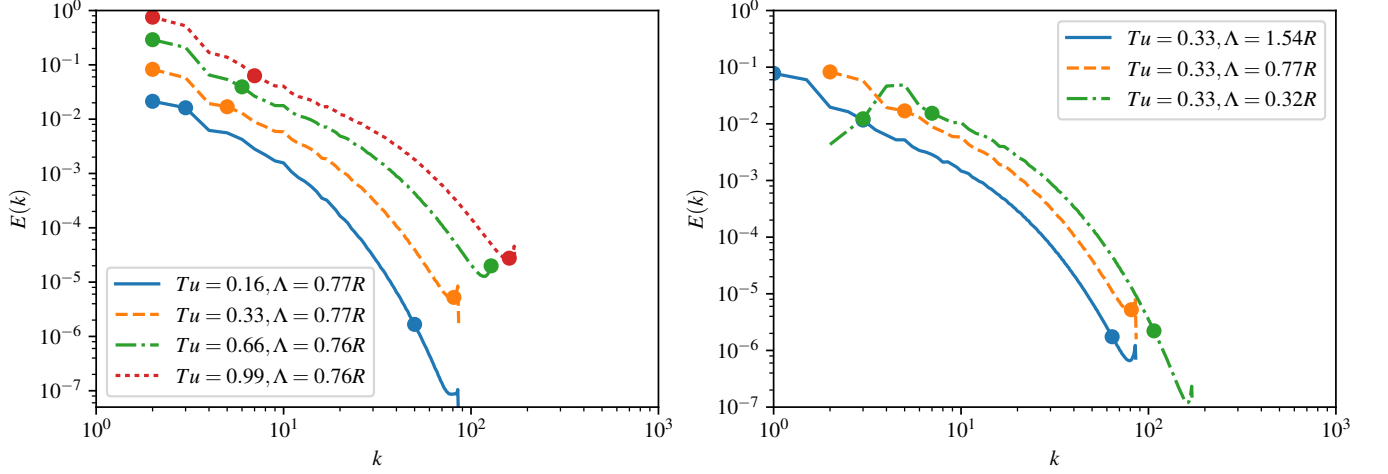


Figure 3. Spectra of turbulent kinetic energy for HIT fields averaged over several eddy turnover times. Left: series A with constant Λ and variable Tu , right: series B for $Tu = 0.33$ and Λ variable. Markers are the wavenumbers associated with Λ , λ and η (from left to right on each spectrum).

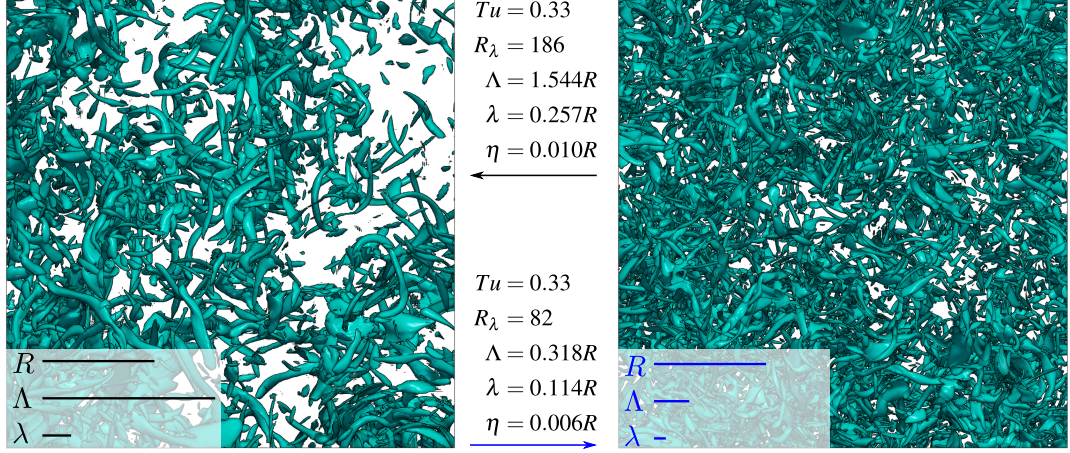


Figure 4. Two HIT fields from the series B, both with identical turbulent kinetic energy (and hence turbulence intensity Tu). Visualized is the isosurface $|\underline{\omega}| = 4\sigma(\underline{\omega})$ of vorticity magnitude, where σ is the standard deviation. Insets show visual comparison of wing length R , integral scale Λ and Taylor micro scale λ .

156

C. Bumblebee model

In our numerical simulations, we use a model bumblebee in forward flight at $u_\infty = 2.5 \text{ m/s}$ as archetype for medium-sized insects. The Reynolds number is $\text{Re} = \bar{U}_{\text{tip}} c_m / \nu_{\text{air}} = 2060$, where $\bar{U}_{\text{tip}} = 2\Phi R f = 8.05 \text{ m/s}$ is the mean wingtip velocity, $c_m = 4.012 \text{ mm}$ the mean chord length, $\nu_{\text{air}} = 1.568 \cdot 10^{-5} \text{ m}^2/\text{s}$ is the kinematic viscosity of air, $R = 1.32 \cdot 10^{-2} \text{ m}$ is the wing length, $f = 152 \text{ Hz}$ ($T = 1/f = 6.6 \text{ ms}$) is the wingbeat frequency (T is duration) and $\Phi = 115^\circ$ is the wingbeat amplitude. The model is described in greater detail elsewhere [18, suppl. mat.]. The mass of the insect is $m = 175 \text{ mg}$, the gravitational acceleration $g = 9.81 \text{ m/s}^2$ and the moments of inertia of the body are $J_{\text{roll}}^{(b)} = 1.14 \cdot 10^{-9} \text{ kg m}^2$, $J_{\text{yaw}}^{(b)} = 4.33 \cdot 10^{-9} \text{ kg m}^2$ and $J_{\text{pitch}}^{(b)} = 4.18 \cdot 10^{-9} \text{ kg m}^2$. We use the superscript $\cdot^{(b)}$ when referring to the body reference frame.

We perform two types of simulations, one where the insect is anchored to the virtual wind tunnel (tethered flight) and one where its motion is computed from fluid forces and moments (free flight) as well as gravity. The governing equation for the free flight case is Newton's second law of motion for linear and angular motion. For the latter, we use a quaternion Ansatz to avoid the Gimbal lock problem. Gimbal lock occurs when two rotation axis become parallel and the system loses one degree of freedom. The detailed set of 13 first-order ODEs can be found in [20]. In both free and tethered flight, we prescribe an identical wing motion relative to the body, as illustrated in Fig. 5. The wing motion is identical for all wing beats. The wings and body

are assumed to be rigid.

Our bumblebee model responds in the free flight case, unlike real animals, entirely passively to perturbations. Therefore, we limit the simulation time to the order of magnitude of the reaction time delay τ_{react} in those animals. After this delay, the insect may employ active steering mechanisms and modify the wing beat or body posture. Previous studies on freely flying honeybees reported response delays of approximately 20ms or 4.5 stroke cycles, suggesting the use of ocellar pathways for body stability reflexes in this species [58]. By contrast, recent work [2] suggests reaction times of about 5 ms in fruit flies. The precise delay in bumblebees is unknown but expected to be of the same order of magnitude as in honeybees. Therefore, we simulate 8 stroke cycles (52.6ms) in a simulation, allowing thus to quantify the response for any $\tau_{\text{react}} \leq 8T$. Notably, we do not exactly know under which conditions insects react at all to perturbations, or simply accept the externally imposed change in flight direction and orientation. An example for this is shown in [51], where bumblebees are found to ignore aerial perturbations when approaching a cylinder.

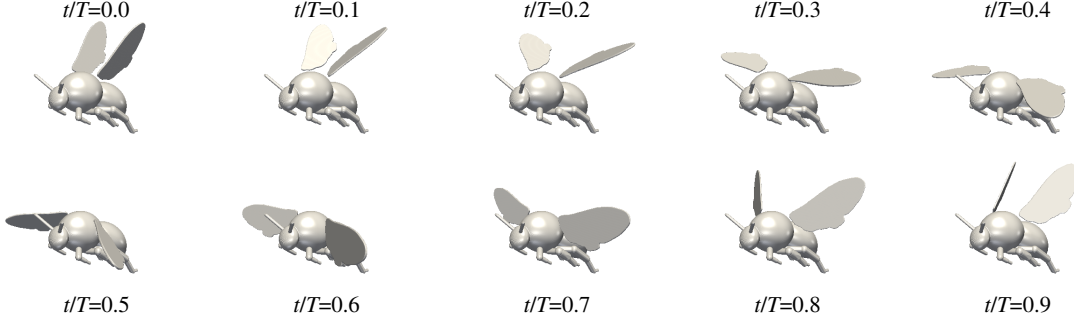


Figure 5. Visualization of the bumblebees prescribed flapping motion every $0.1T$ time steps.

D. Governing equations and numerical method

The present work relies on numerical simulations. We directly solve the incompressible Navier–Stokes equations without any *a priori* turbulence models. All scales of fluid motion are fully resolved in time and space. In this section, we describe briefly the numerical method we use, for reasons of self-consistency. For further details the reader is referred to [20].

We employ a Fourier pseudospectral method for spatial discretization and a 2nd order Adams-Bashforth scheme for time advancement. The spectral discretization is fast and accurate [46] and is particularly useful in our case as the Laplace operator becomes diagonal in Fourier space. Hence, the solution of a Poisson problem is trivial in Fourier space. To include the no-slip boundary conditions on the time-varying geometry we use the volume penalization method [1]. This allows us to maintain the advantages of the Fourier discretization. Hence, we solve the penalized Navier–Stokes equation

$$\partial_t \underline{u} + \underline{\omega} \times \underline{u} = -\nabla \Pi + \nu \nabla^2 \underline{u} - \underbrace{\frac{\chi}{C_\eta} (\underline{u} - \underline{u}_s)}_{\text{penalization}} - \underbrace{\frac{1}{C_{\text{sp}}} \nabla \times \frac{(\chi_{\text{sp}} \underline{\omega})}{\nabla^2}}_{\text{sponge}} \quad (1)$$

$$\nabla \cdot \underline{u} = 0 \quad (2)$$

$$\underline{u}(\underline{x}, t = 0) = \underline{u}_0(\underline{x}) \quad \underline{x} \in \Omega, t > 0, \quad (3)$$

where \underline{u} is the fluid velocity, $\underline{\omega} = \nabla \times \underline{u}$ is the vorticity. We normalize the density ρ_f to unity. The nonlinear term in eqn. (1) is written in the rotational form. Hence we are left with the gradient of the total pressure $\Pi = p + \frac{1}{2} \underline{u} \cdot \underline{u}$ instead of the static pressure p [46]. This formulation is chosen because of its favorable properties when discretized with spectral methods, namely conservation of momentum and energy [46, pp. 210]. At the exterior of the computational domain, we assume periodic boundary conditions. The domain is sufficiently large to minimize the effect of periodicity.

The mask function χ is defined as

$$\chi(\underline{x}, t) = \begin{cases} 0 & \text{if } \underline{x} \in \Omega_f \\ 1 & \text{if } \underline{x} \in \Omega_s \end{cases}, \quad (4)$$

where Ω_f is the fluid and Ω_s the solid domain. Note that in the fluid domain Ω_f , the original equations hold as the penalization term $\frac{\chi}{C_\eta} (\underline{u} - \underline{u}_s)$ vanishes. The convergence proof in [1, 4] shows that the solution of the penalized Navier–Stokes equations (1-3) tends for $C_\eta \rightarrow 0$ indeed towards the exact solution of Navier–Stokes imposing no-slip boundary conditions. Here, we use

199 $C_\eta = 2.5 \cdot 10^{-4}$. We also add a second penalization term for the vorticity $\underline{\omega}$, which we call sponge term. The sponge gradually
 200 damps the vorticity in regions where $\chi_{\text{sp}} = 1$. The sponge constant is set to $C_{\text{sp}} = 10^{-1}$.

201 In the case of free flight, we compute the position and orientation of the insect from the aerodynamic forces and moments
 202 using a quaternion-based formulation. We integrate the resulting ODE system time using the same Adams-Bashforth scheme as
 203 for the fluid. More details about the numerical method and its implementation in the open-source code FlUSI [42] can be found
 204 in [20], along with detailed validation cases. In addition, appendix A shows the convergence of the forces for decreasing wing
 205 thickness of a flapping wing.

III. RESULTS AND DISCUSSION

207 In the following subsection, we present and discuss the results of two types of simulations, tethered and free flight. We use
 208 both cases to investigate the influence of turbulence on the insect when varying either the intensity or the length scales of the
 209 turbulent inflow perturbations. We start with the tethered cases, which serves as reference for the free flight cases. In numerical
 210 simulations, the tethered case is the idealized limit of perfect control. In experimental work, where the animals are fixed using a
 211 material tether, usually a thin wire glued to the back, the insects lack sensor feedback present in free flight. The wing kinematics
 212 might then be very different from what an insect uses in free flight [54]. However, note that our tethered simulations are based
 213 on wing kinematics measured in free flight [14, 15]. They are thus equivalent to a tethered insect that flaps as if it was in free
 214 flight.

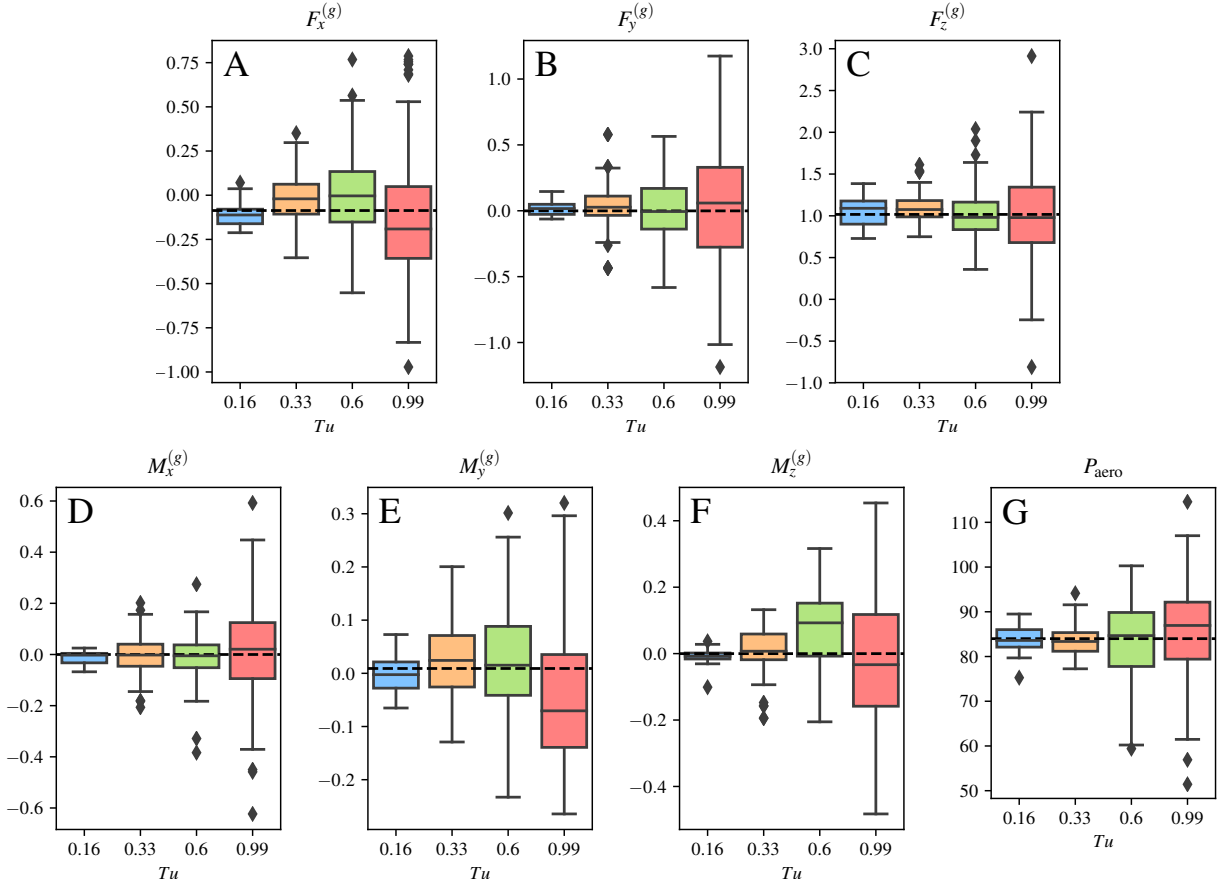


Figure 6. Tethered flight in turbulence. The integral scale is $\Lambda = 0.77R$ and Tu varies between 0 and 0.99. Cycle averaged values are represented by box plots. Each of the N_R simulations yields 4 data points, one for each cycle. In the colored boxes, the line is the median (or 2-quantile) of the data, and the limits of the box are the upper and lower quartiles (or 4-quantile). The additional vertical line are min/max values excluding outliers, which are shown as individual points with a \diamond marker. Aerodynamic quantities are forces (A-C, normalized by mg), moments (D-F, normalized by mgR) and aerodynamic power (G, in W/kg body mass). The dashed line corresponds to the laminar case ($Tu = 0$) where the insect is aligned with the mean flow.

A. Tethered flight

1. Influence of turbulence intensity at fixed length scales

We first study the influence of Tu at constant integral scale Λ . The insect is tethered and we used the series A of turbulence fields, as presented in [18]. Their properties are summarized in Table I. We fix the integral scale and vary the turbulence intensity Tu , which also results in an increasing Reynolds number R_λ and reduced eddy turnover time. Fig. 6 illustrates the obtained results for forces (A-C), moments (D-F) and aerodynamic power (G). We choose the box plot representation, first introduced in [57], to visualize the data. Each of the N_R realizations yields N_w independent cycle-averaged forces and moments (Table I). The median value of the data are remarkably close to the value in the laminar case (dashed line) for all quantities, even in the strongest inflow turbulence. This indicates that turbulence does not systematically alter the vortex dynamics generated by the flapping wings of the insect. This vortex system features the leading edge vortex that results from the typically high angle of attack (here roughly 50°) [16, 17, 33]. The leading edge vortex remains attached to the wing in unperturbed conditions, and in the simulations with turbulent inflow it is not systematically detaching neither. Owing to the decreased pressure in its core, this vortex provides a boost for the aerodynamic forces, especially the lift force. Thus, its detachment or destruction would result in a significant change in forces, moments and power. Compared to an airfoil, where upstream turbulence can trigger transitions in the boundary layer or impact flow separation, this behavior is thus different. However, fluctuations occur, as represented in Fig. 6 by the colored boxes and the min/max values. With increasing turbulence intensity, those fluctuations become larger. We conclude that flapping flight in turbulence faces insects more with a problem for control, rather than deteriorated force production [18].

2. Influence of turbulent length scales at constant intensity

With the results of [18] we now further explore the influence of turbulent length scales on tethered flight and use the series B from Table I, where we fixed $Tu = 0.33$. This particular intermediate value of Tu does not require a large number of flow realizations for any tested value of Λ , which allows keeping the computational cost within acceptable limits. Furthermore, field experiments [11] show a large flight activity of bumblebees for this value of Tu .

Fig. 7 illustrates the cycle-averaged forces, moments and power as a function of Λ . The median values are close to the values in laminar inflow (dashed line), which is consistent with the findings in [18] and Fig. 6. For any quantity, fluctuations are significantly reduced at $\Lambda = 0.32R$ (blue), compared to the other two cases. The lateral (Fig. 7B) and lift (Fig. 7C) force exhibit the largest fluctuations for $\Lambda = 0.77R$, while the fluctuations in thrust (Fig. 7A) are of the same magnitude in both cases. For the aerodynamic torques (Fig. 7D-F) largest fluctuations appear for $\Lambda = 1.54R$ with standard deviation $\sigma = 0.104, 0.095, 0.076$ for the roll (M_x), pitch (M_y) and yaw (M_z) moments, respectively. The yaw moment is slightly less sensitive to perturbations but remains of the same order of magnitude. The aerodynamic power P_{aero} (Fig. 7G) displays the same behavior as the forces, with $\Lambda = 0.77R$ resulting in the largest fluctuations. However, in that case, $\sigma(P_{\text{aero}})/\bar{P}_{\text{aero}} = 0.05$, while for the vertical force $\sigma(F_z)/\bar{F}_z = 0.2$. The power thus fluctuates little.

These results suggest a reduced sensitivity to turbulence at smaller scales, expressed in a reduction of more than a factor of two in the magnitude of fluctuations at the same turbulence intensity. This is in agreement with the conjecture stated in [50] that perturbations which are small compared to the animal average out over the body and thus induce less perturbations. To further explore the effect of Λ , we illustrate in Fig. 8A-B the flow for the coarsest and finest turbulent case. Vortical structures are visualized by the Q-criterion [29]. For both inflow conditions, we plot the same relative isosurface using the standard deviation σ , $Q = 0.7\sigma(Q)$, to identify vortices. In the coarser turbulence, less vortex tubes can be identified in the region between the inlet and the insect than in the smaller scale case, and the tubes are of similar diameter. This may lead to the visual intuition that the smaller scale turbulence has a larger impact on the insect. However, the pressure field, illustrated in Fig. 8C-D as the difference in pressure between the turbulent and laminar realization, $\Delta p = p_{\text{turb}} - p_{\text{lam}}$, confirms that pressure fluctuations are of similar magnitude in both cases, while the spatial scale differs significantly. The coarser scale turbulence is associated with much larger scales of the pressure variations, which therefore have less chance of canceling out over the region of the insect.

B. Free flight

We now consider our model in free flight with all six degrees of freedom coupled to the flow solver, neglecting active control. This configuration is more realistic for real insects, since they cannot react instantaneously to changes in the flow condition. Reaction rather takes place after a time delay τ_{react} , during which sensor information are converted to changes in wing beat for active countermeasures (see section II C). Therefore, the insect behaves passively during this interval, similar to what our model does. The orientation and linear/angular velocities after τ_{react} can thus yield insight into the effort required for corrective maneuvers.

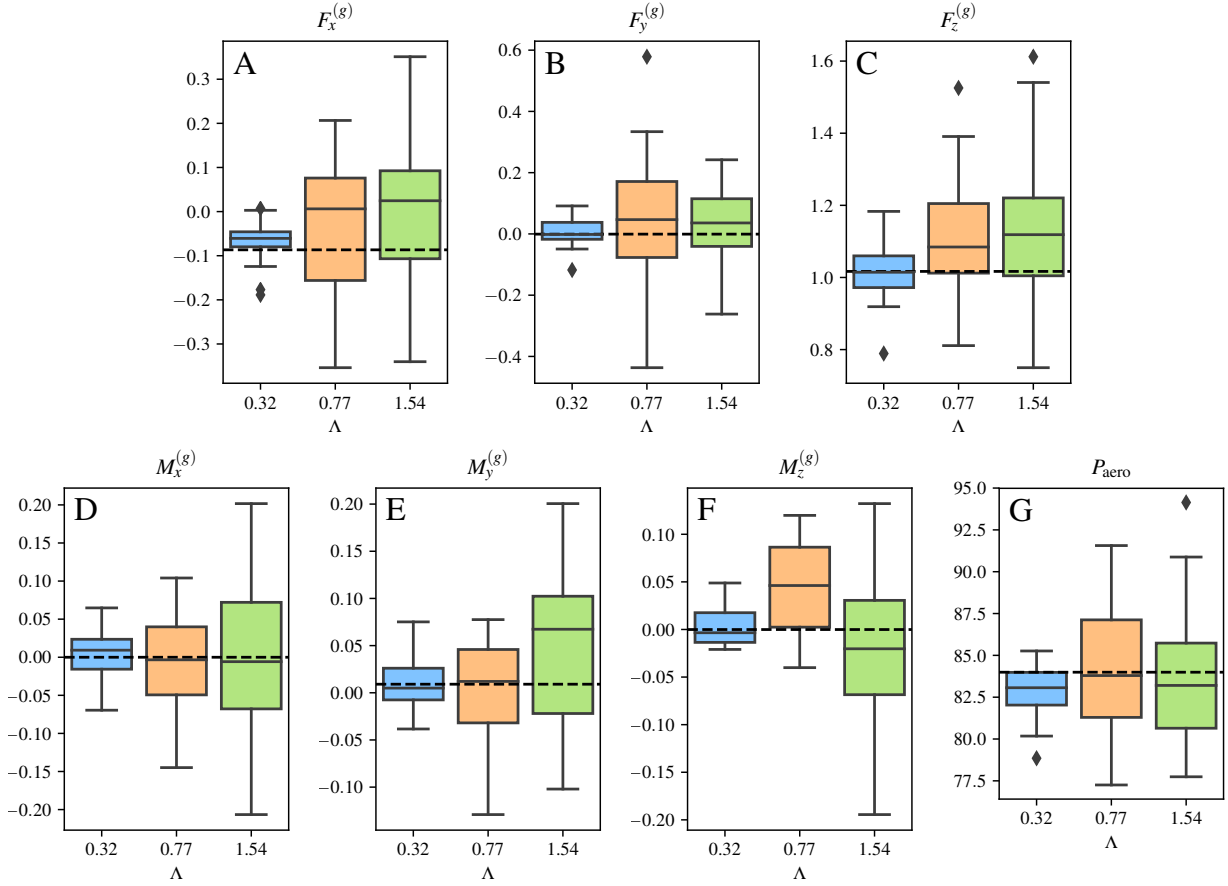


Figure 7. Tethered flight in turbulence. The turbulence intensity is $Tu = 0.33$ and the integral scale Λ varies between $0.32R$ and $1.54R$. Cycle averaged values are represented by box plots. Each of the N_R simulations yields 4 data points, one for each cycle. In the colored boxes, the line is the median of the data, and the limits of the box are the upper and lower quartiles. The additional vertical line are min/max values excluding outliers, which are shown as individual points with a \diamond marker. Aerodynamic quantities are forces (A-C, normalized by mg), moments (D-F, normalized by mgR) and aerodynamic power (G, in W/kg body mass). The dashed line corresponds to the laminar case ($Tu = 0$) where the insect is aligned with the mean flow.

265

1. Influence of turbulence intensity at constant length scales

After revisiting the problem of a tethered bumblebee in turbulence and studying the same model in free flight and laminar inflow, we now turn to free flight in turbulence. We first keep $\Lambda = 0.77R$ fixed for these simulations and alter the energy content of the imposed velocity fluctuations (series A in Table I). In free flight, force and moment fluctuations are transduced to linear and angular velocities, which in turn alter the forces and moments. It can be seen as the limiting case of no flight control, while tethered flight can somehow be seen as limit of perfect control using external force, in the sense that attitude is perfectly stabilized while neglecting the necessary changes in wing beat.

Fig. 9A-D shows the magnitude of the body's angular velocity, $\Omega_b^{(b)}$, as a function of time for the four different turbulence intensities $Tu = 0.16, 0.33, 0.60$ and 0.99 . At the lowest turbulence intensity (Fig. 9A), fluctuations remain small and the overall time evolution resembles the laminar case, in which only the pitch component of $\underline{\Omega}_b^{(b)}$ is nonzero owing to lateral symmetry, although the difference grows in time. The first stroke is virtually unaffected as perturbations have not yet been advected to the insect. From the next larger value of Tu on (Fig. 9B), the resemblance to the laminar case disappears. The terminal value of the ensemble averaged angular velocity increases from $829^\circ/\text{s}$ at $Tu = 0.33$ (Fig. 9B) to $2300^\circ/\text{s}$ at $Tu = 0.99$ (Fig. 9D). In the laminar case, peak values of $470^\circ/\text{s}$ are found. It can be seen that after an initial growth phase, which takes place roughly in the first two strokes, the average angular velocity remains roughly constant, thus it is limited by aerodynamic damping.

Fig. 10 shows the components of the angular velocity vector, averaged over the last cycle $7 \leq t/T \leq 8$, as a function of the turbulence intensity. The magnitude of the mean value as well as fluctuations increase with increasing Tu , but no relevant difference among the three directions can be observed. We thus do not observe a significantly increased roll angular velocity (Fig. 10C), despite the lower moment of inertia around this axis.

283

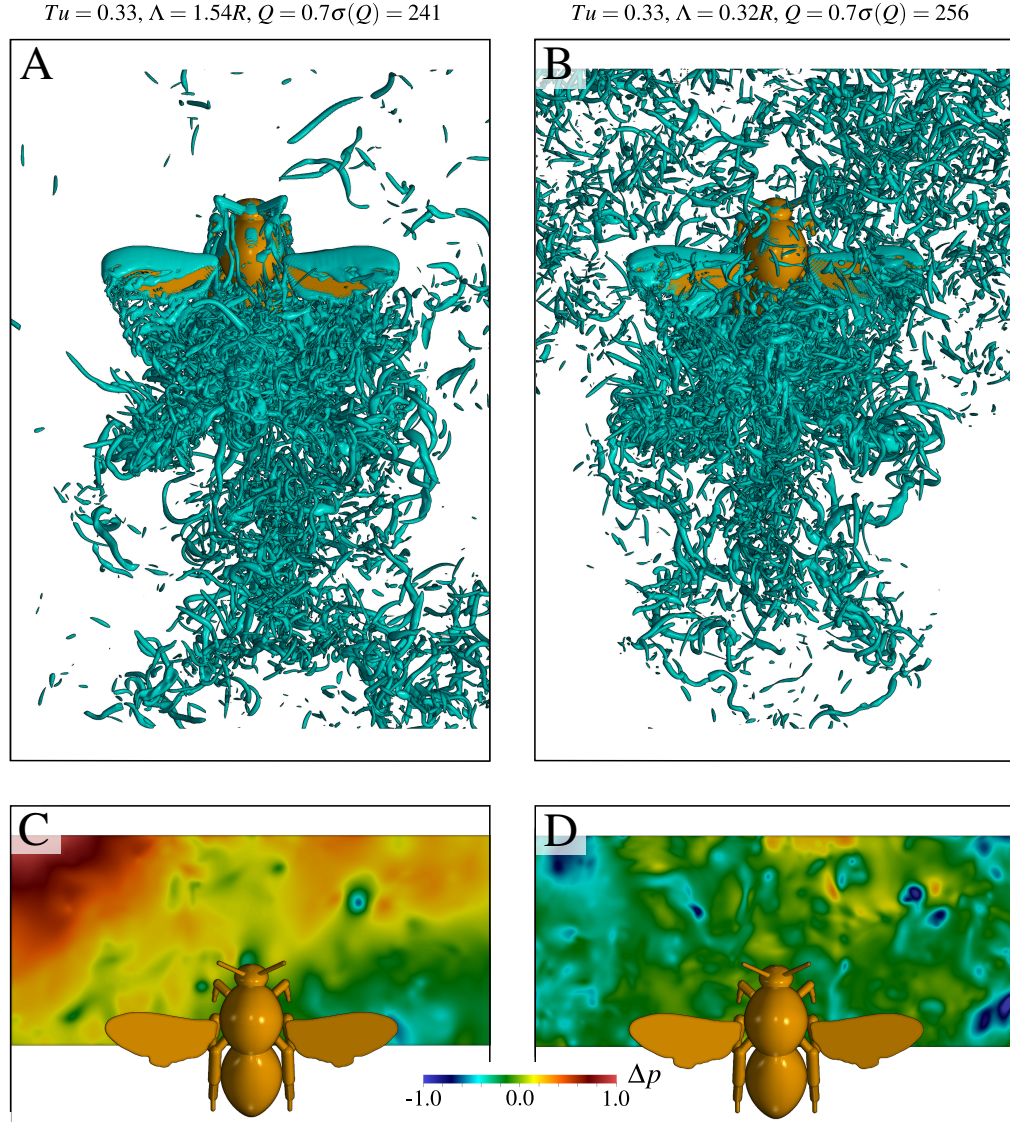


Figure 8. Tethered flight in turbulence. Left column: $Tu = .33$ and $\Lambda = 1.54R$, right column: $Tu = .33$ and $\Lambda = 0.32R$. (A-B) An isosurface of the Q -criterion is shown to visualize vortical structures. In the case of $\Lambda = 1.54R$ (A), fewer vortices are identified upstream of the insect. (C-D) show the corresponding pressure field, where the pressure from the laminar inflow has been subtracted, $\Delta p = p_{\text{turb}} - p_{\text{lam}}$. Compared to the $\Lambda = 0.32R$ case (D), variations in pressure are of the same order of magnitude but on a larger spatial scale in the $\Lambda = 1.54R$ case (C).

284 We find the largest magnitude of linear velocity $\left| \underline{u}_b^{(b)} \right| / u_\infty = 0.06 \pm 0.04$ for the highest turbulence intensity ($Tu = 0.99$,
 285 $\Lambda = 0.77R$). It can be concluded that, even for the largest turbulence intensity, the translational response of the bumblebee is
 286 small compared to the flight speed. Therefore, the changes in position $\underline{x}_{\text{cntr}}$ are small within the time span of the computations,
 287 *i.e.* $8T$. The impact of turbulence on the angular degrees of freedom is thus much higher than on the linear ones.

2. Influence of turbulent length scales at constant intensity

289 As for the tethered case, we fix $Tu = 0.33$ and vary the integral scale Λ of the turbulent inflow perturbations. Fig. 11 shows
 290 the angular velocity components for the case $Tu = 0.33$, $\Lambda = 0.77R$ (A–C) and $\Lambda = 0.32R$ (D–F). Each realization is shown
 291 as a thin gray line, the reference computation in laminar flow is shown as red dashed line. All realizations result in a different
 292 attitude of the insect, though the turbulence fields have identical statistical properties. The ensemble-averaged time evolution
 293 (solid green lines) is however remarkably close to what is seen in laminar inflow. Standard deviations among the realizations
 294 (green shaded area) increase with time, as turbulent inflow perturbations are imposed continuously.

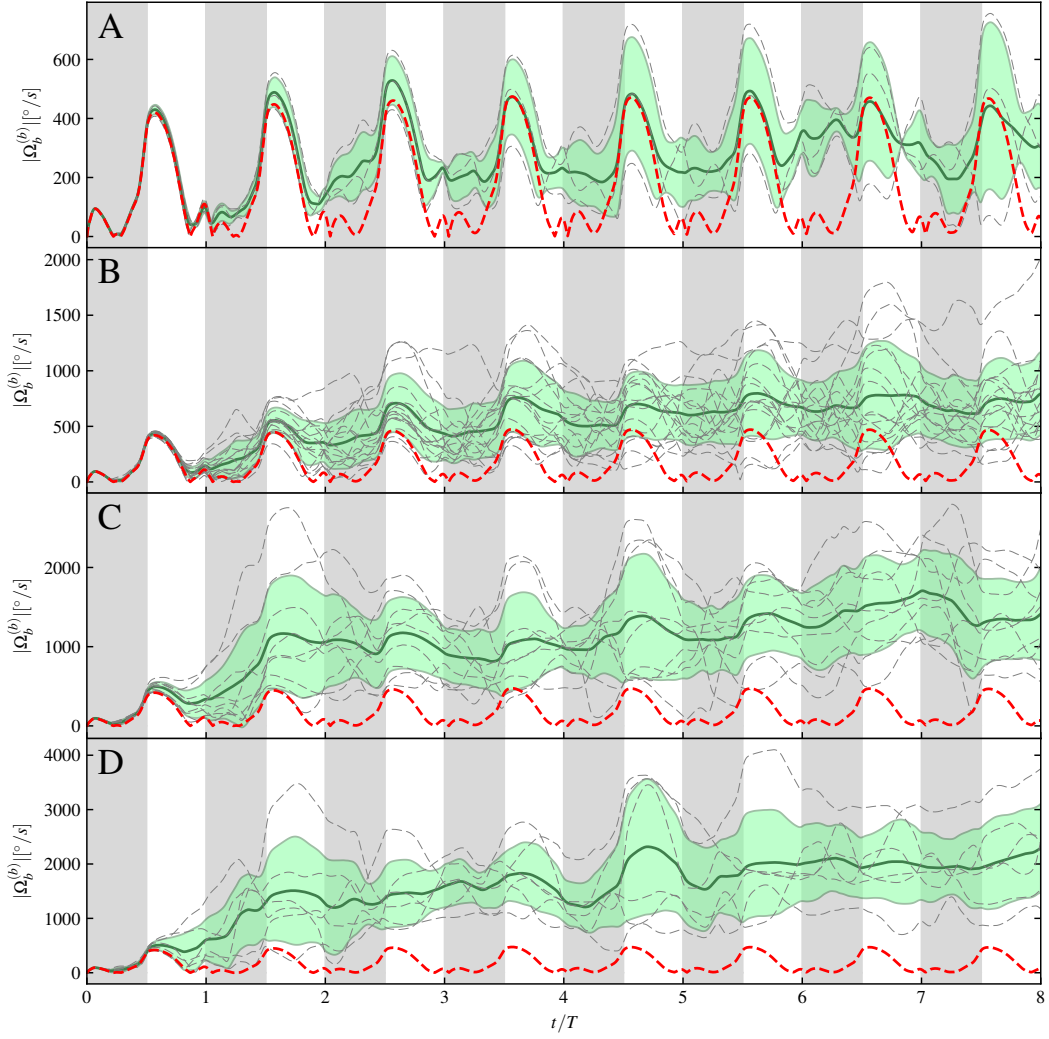


Figure 9. Free flight in turbulent inflow, $Tu = 0.16$ (A), 0.33 (B), 0.60 (C) and 0.99 (D), for fixed $\Lambda = 0.77$. Time evolution for the magnitude of body angular velocity. Individual realizations are shown as thin, gray, dashed lines. Ensemble averaged time evolution is represented by the thick green line, light green shaded background illustrates the standard deviation. The red dashed line corresponds to the laminar case.

Ensemble averaged angular orientation, expressed in term of the body angles, does not change significantly for ψ_{roll} and ψ_{yaw} , while β_{pitch} has changed by 8.5° . Fluctuations are largest for yaw (15.4°), followed by pitch (11.0°) and roll (10.3°). The values are however close to each other, such that the difference is not significant.

For all components, the standard deviation of the angular velocity $\underline{\Omega}_b^{(b)}$ first grows in time, until some saturation is reached. The initial growth rate is largest for the roll component (Fig. 11A), which presents large fluctuations at $t = 2T$ already. By this time, the pitch component (B) has almost vanishing fluctuations and those in yaw (C) are significantly smaller. The insects motion is damped by the viscous fluid, and thus the magnitude of the angular velocity remains bounded.

Fig. 11D–F show the same quantities as Fig. 11A–C for the case $\Lambda = 0.32R$. While the qualitative behavior is similar, the magnitude of both changes in angular orientation and angular velocities of the body ($\underline{\Omega}_b^{(b)}$) are significantly reduced. For example, $\gamma_{\text{yaw}} = 20^\circ$ in the $\Lambda = 0.77R$ case is reduced to 2.5° . The fluctuations in roll angular velocity grow fastest.

From the direct comparison of the two cases we can confirm the conclusions from the tethered simulations also in the free flight case. The reduced integral scale significantly reduces the impact of the flow on the insect's attitude. Fig. 12 shows the magnitude of the different components of the angular velocity and confirms that conclusion. Furthermore, as the 95% confidence intervals of the different directions overlap for both values of Λ , again no direction with statistically significantly increased magnitude can

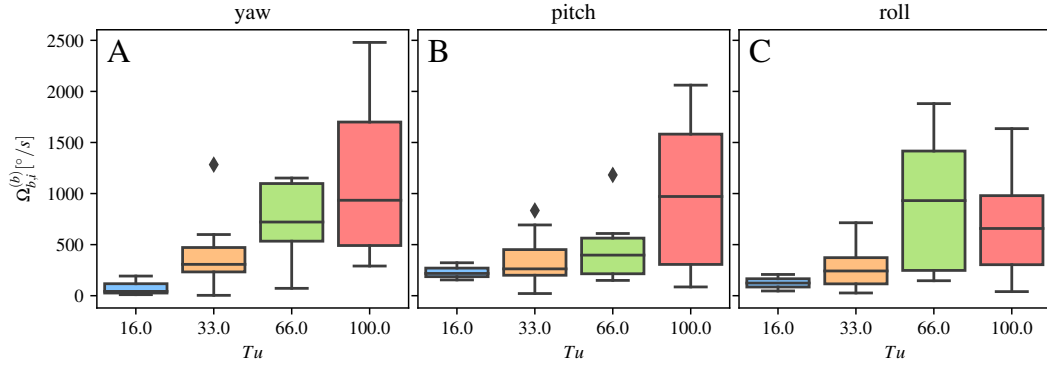


Figure 10. Free flight in turbulent inflow. Shown are the yaw (A), pitch (B) and roll (C) components of the body angular velocity, averaged over the last computed cycle, as a function of the turbulence intensity. Data are represented by a box plot. In the colored boxes, the line is the median of the data, and the limits of the box is the upper and lower quartiles. The additional vertical line correspond to min/max values excluding outliers (\diamond).

be observed. It appears thus from Fig. 11 that while the roll angular velocity grows fastest, its terminal value is not significantly larger than the other two components, yaw and pitch.

A key advantage of numerical work is that we can exclude any voluntary motion that might be used, *e.g.*, for distance estimation [51]. However, at this point, we cannot give a quantitative estimate for the limit of stable flight in turbulent conditions. The first uncertainty concerns the degree of desired control. Experimental work [51] suggests that bumblebees passively ride out small scale perturbations and actively impose a long wavelength casting motion. It thus seems that real animals are somewhat behaving between the two limiting cases of tethered and free flight. This can also result from energetic considerations as allowing for a certain amount of deviations may reduce overall energetic cost.

The role of the reaction time delay appears to be the second crucial factor for evaluating the stability. Our free flight data shows that fluctuations in angular velocity grow fastest for the roll axis, which is a consequence of the reduced moment of inertia. Figs. 11A and C show that the roll component has reached its saturation at about $t = 2T$. Beyond this time, damping inhibits further growth, possibly via the flapping counter torque (FCT) mechanism [25, 26]. This does not imply any bound for changes in body angles, which continuously grow in time. However, without the damping, the angular velocities are expected to grow continuously, leading to much greater changes in orientation.

Experimental work [58] showed that honeybees (*Apis mellifera*) use angular velocities for roll, pitch and yaw of 3090 , 697 , $1874^\circ/s$, respectively, during the active recovery phase after being perturbed with a strong wind gust. The magnitude of this angular velocity is $3680^\circ/s$, which is higher than the largest value we find in our simulations (Fig. 9), and also higher than the $2060^\circ/s$ which [58] reports during the passive phase directly after the perturbation. The associated reaction time is stated as $3.5T < \tau_{\text{react}} < 6T$. Besides differences in species (we are not aware of data available for bumblebees in the literature), the study cannot directly be used to define a threshold for the angular velocity beyond which the animals cannot recover. In addition, flying in turbulence imposes continuous perturbations, while [58] studied the effect of a singular gust.

IV. CONCLUSIONS AND PERSPECTIVES

We numerically studied the impact of turbulence on a model insect, using high-resolution numerical simulations on massively parallel machines. Both tethered and free flight without control have been considered, using a bumblebee model with rigid wings and prescribed wing beat kinematics. The inflow condition ranged from laminar to turbulent, and in the latter we varied the turbulence intensity as well as the spectral distribution of the turbulent kinetic energy. For the turbulent inflows, we performed ensemble-averaging to obtain statistical estimates of forces, moments and power in tethered case and body orientation and velocities in the free flight case.

In tethered flight, we have statistically estimated that the turbulent inflow does not induce the detachment of the leading edge vortex. This is true even in the strongest turbulence case and has already been shown in our previous work [18]. In addition to the turbulence intensity, here we found the spectral distribution of turbulent kinetic energy to be a significant parameter to be taken into account. If the integral scale of the inflow is smaller than the wing length, we found that statistically perturbations are reduced for forces, moments and power, compared to turbulent inflow with larger integral scale. We have demonstrated that the pressure field of the turbulent perturbations is associated likewise with large scale variations if the integral scale is large. The positive and negative pressure perturbations have thus less chance of canceling out over the body, which induces larger fluctuations.

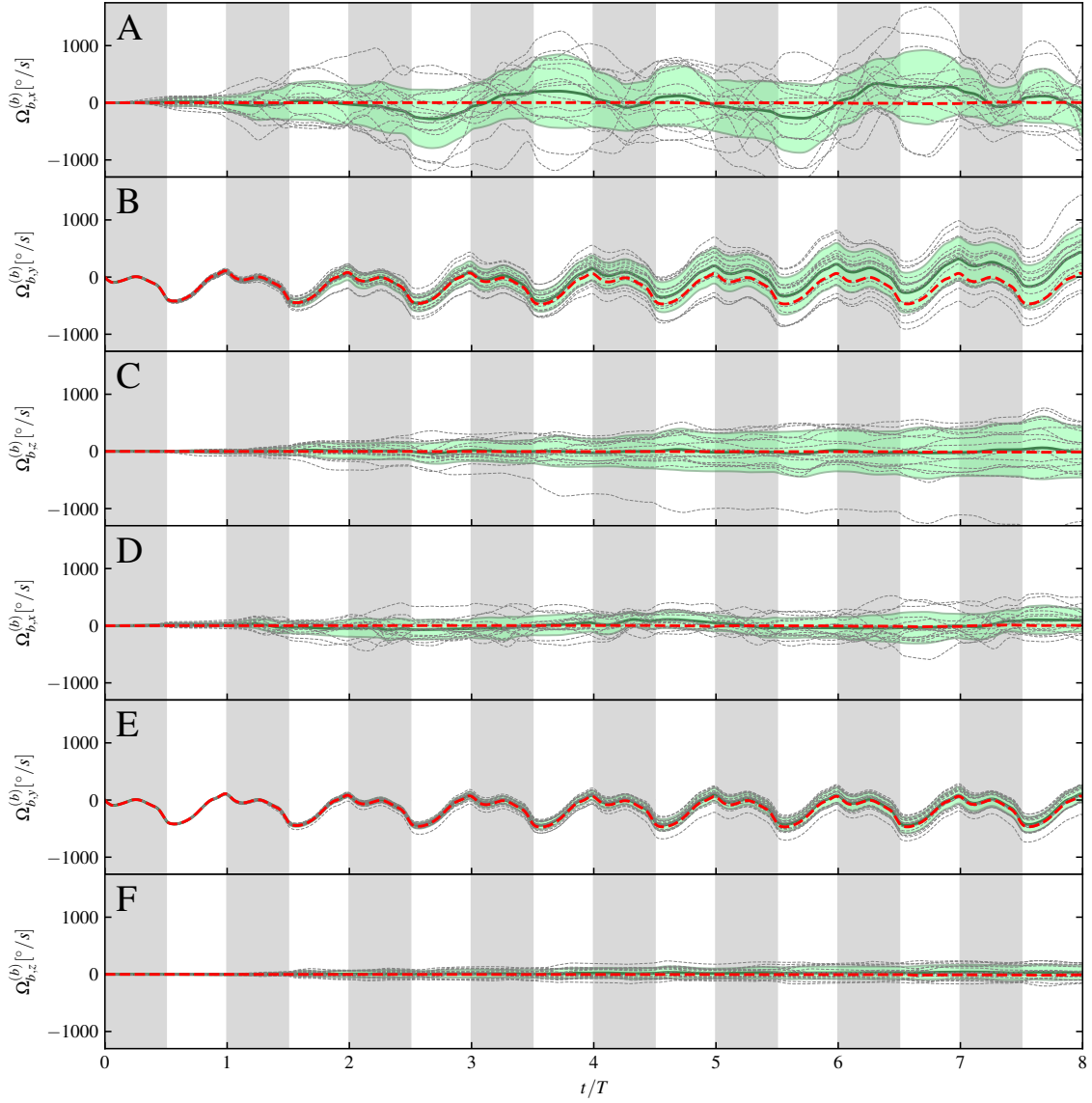


Figure 11. Free flight in turbulent inflow, $Tu = 0.33$, A–C: $\Lambda = 0.77R$, D–F: $\Lambda = 0.32R$. Time evolution of the three components of the angular velocity vector of the body, in the body system $\underline{\Omega}_b^{(b)}$. Angular velocities are given in $^\circ/s$ for easier comparison with results in the literature. Individual realizations are shown as thin gray lines. Ensemble averaged time evolution is represented by the thick green line, light green shaded background illustrates the standard deviation. The thick red dashed line corresponds to the laminar case.

Using free flight simulations we first checked that our model remains stable for laminar inflow condition. In turbulent inflow, we confirmed the finding from the tethered flight. We found that changes in body orientation and angular velocity are highly sensitive to variations in the turbulence spectrum. For constant turbulence intensity, a smaller integral scale results in much smaller angular velocities and changes in orientation. By modifying the turbulence intensity at fixed integral scale, we showed how the angular velocities increase when the perturbations become stronger. In all free flight simulations, we found the translation of the insect to be small compared to its rotational motion.

Collectively, our findings suggest that the scales of turbulent motion have a significant effect on the aerodynamics of flapping flight and should hence be considered in future contributions on this topic.

In perspective, we plan to overcome the limitations of the current study and specifically include the effects of both wing flexibility and flight control. Moreover, since our results have been obtained using a single species, namely a bumblebee, the

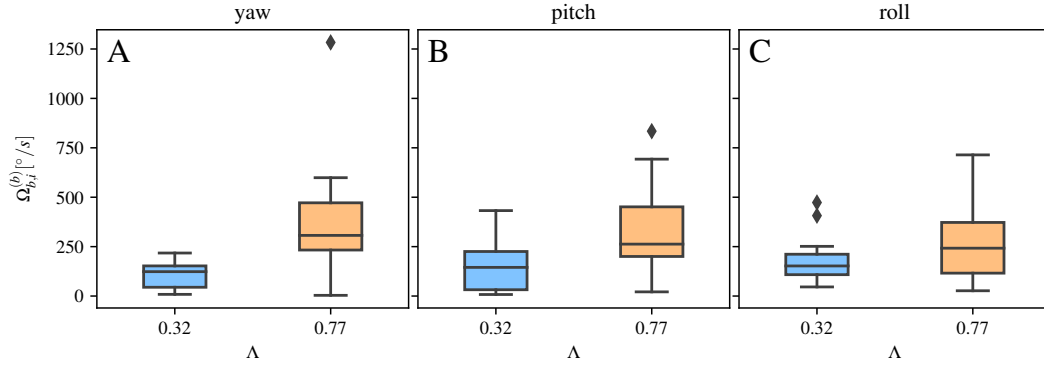


Figure 12. Free flight in turbulent inflow. Yaw (A), pitch (B) and roll (C) components of the body angular velocity, averaged over the last computed cycle, as a function of Λ . Data are represented by a box plot. In the colored boxes, the line is the median of the data, and the limits of the box is the upper and lower quartiles. The additional vertical line is min/max values excluding outliers (\diamond).

generalization to other insects is another important direction for future work. Finally, we aim to replace the homogeneous isotropic turbulence, which is a valuable starting point, by generic turbulent flows even more relevant to insects, e.g., flower wakes.

ACKNOWLEDGMENTS

Financial support from the Agence nationale de la recherche (ANR Grant 15-CE40-0019) and Deutsche Forschungsgemeinschaft (TE, JS: DFG Grant SE 824/26-1, FL: Grant LE905/17-1), project AIFIT, is gratefully acknowledged. This work was granted access to the HPC resources of IDRIS under the allocation 2018-91664 attributed by GENCI (Grand Équipement National de Calcul Intensif). For this work we were also granted access to the HPC resources of Aix-Marseille Université financed by the project Equip@Meso (ANR-10-EQPX- 29-01). TE, KS, MF, FL and JS thankfully acknowledge financial support granted by the ministères des Affaires étrangères et du développement International (MAEDI) et de l'Education national et l'enseignement supérieur, de la recherche et de l'innovation (MENESRI), and the Deutscher Akademischer Austauschdienst (DAAD) within the French-German Prococpe project FIFIT.

I. APPENDIX: CONVERGENCE TO AN INFINITESIMALLY THIN FLAPPING WING

In this appendix, we study the convergence of our numerical scheme in the limit of infinitesimally thin wings. We choose the same wing geometry as in the rest of the article, with the same kinematics, but simulate only one wing without the insects body. The domain size is reduced to $2 \times 2 \times 2$ in order to be able to reach high resolutions. The thickness of the wing is $h_w/R = c_t \Delta x$ where we set the constant $C_t = 4$. As no reference solution is available, we instead use the solution on the finest grid. As described in [20], the penalization parameter $C_\eta = (K_\eta \Delta x)^2 / \nu$ is reduced with increasing resolution, in order to achieve optimal results. The constant is $K_\eta = 7.4 \cdot 10^{-2}$. We perform five simulations with resolution 192^3 , 384^3 , 512^3 , 768^3 and 1024^3 , with h_w/R ranging from 4.2% to 0.78%. The error is evaluated as

$$\varepsilon = \int_0^{2T} (F_i - F_{\text{ref},i}) dt / \int_0^{2T} F_{\text{ref},i} dt.$$

Fig. 13 shows the resulting convergence. For all components, we find qualitatively the same behavior and an order of about 1.5. We can hence conclude that the penalization method retains its accuracy also in the limit of thin flapping wings.

-
- [1] P. Angot, C. Bruneau, and P. Fabrie. A penalization method to take into account obstacles in incompressible viscous flows. *Numer. Math.*, 81:497–520, 1999.
 - [2] T. Beatus and I. Cohen. Wing-pitch modulation in maneuvering fruit flies is explained by an interplay between aerodynamics and a torsional spring. *Phys. Rev. E*, 92:022712, 2015.
 - [3] R. Berthé and F.-O. Lehmann. Body appendages fine-tune posture and moments in freely manoeuvring fruit flies. *J. Exp. Biol.*, 218(20):3295–3307, 2015.

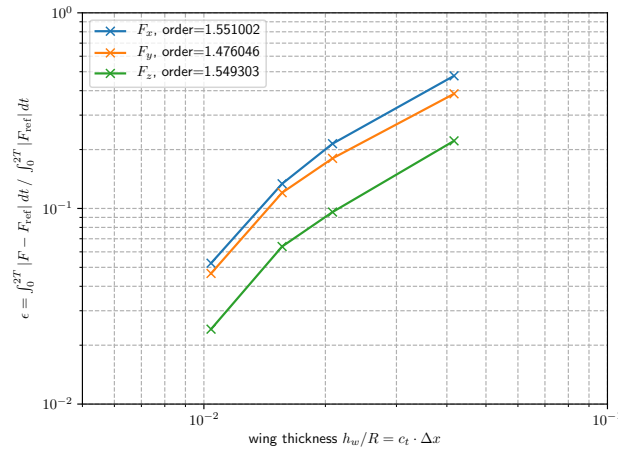


Figure 13. Convergence of forces in the wing thickness.

- [4] G. Carbou and P. Fabrie. Boundary layer for a penalization method for viscous incompressible flow. *Adv. Diff. Equ.*, 8:1453–2480, 2003.
- [5] J. W. Chapman, V. A. Drake, and D. R. Reynolds. Recent insights from radar studies of insect flight. *Annu. Rev. Entomol.*, 56(1):337–356, 2011. PMID: 21133761.
- [6] J.W. Chapman and V.A. Drake. Insect Migration. In *Encyclopedia of Animal Behavior*, volume 2, pages 161–166. Elsevier, 2010.
- [7] B. Cheng and X. Deng. Translational and rotational damping of flapping flight and its dynamics and stability at hovering. *IEEE Trans. Robot.*, 27(5):849–864, 2011.
- [8] B. Cheng, S. N. Fry, Q. Huang, and X. Deng. Aerodynamic damping during rapid flight maneuvers in the fruit fly drosophila. *J. Exp. Biol.*, 213:602–612, 2010.
- [9] S. A. Combes and T. L. Daniel. Flexural stiffness in insect wings I. scaling and the influence of wing venation. *J. Exp. Biol.*, 206:2979–2987, 2003.
- [10] S. A. Combes and R. Dudley. Turbulence-driven instabilities limit insect flight performance. *Proc. Natl. Acad. Sci. USA*, 106:9105–9108, 2009.
- [11] J. D. Crall, J. J. Chang, R. L. Oppenheimer, and S. A. Combes. Foraging in an unsteady world: bumblebee flight performance in field-realistic turbulence. *Interface Focus*, 7(1), 2016.
- [12] M. H. Dickinson and F. T. Muijres. The aerodynamics and control of free flight manoeuvres in drosophila. *Phil. Trans. R. Soc. B*, 371:20150388, 2016.
- [13] R. Dudley. *The biomechanics of insect flight: form, function, evolution*. Princeton University Press, 2002.
- [14] R. Dudley and C. P. Ellington. Mechanics of forward flight in bumblebees I. kinematics and morphology. *J. Exp. Biol.*, 148:19–52, 1990.
- [15] R. Dudley and C. P. Ellington. Mechanics of forward flight in bumblebees II. quasi-steady lift and power requirements. *J. Exp. Biol.*, 148:53–88, 1990.
- [16] C. P. Ellington, C. van den Berg, A. P. Willmott, and A. L. R. Thomas. Leading-edge vortices in insect flight. *Nature*, 384:626–630, 1996.
- [17] C.P. Ellington. The novel aerodynamics of insect flight: applications to micro-air vehicles. *J. Exp. Biol.*, 202:3439–3448, 1999.
- [18] T. Engels, D. Kolomenskiy, K. Schneider, F.-O. Lehmann, and J. Sesterhenn. Bumblebee flight in heavy turbulence. *Phys. Rev. Lett.*, 116:028103, 2016.
- [19] T. Engels, D. Kolomenskiy, K. Schneider, and J. Sesterhenn. Numerical simulation of fluid-structure interaction with the volume penalization method. *J. Comput. Phys.*, 281:96–115, 2015.
- [20] T. Engels, D. Kolomenskiy, K. Schneider, and J. Sesterhenn. FluSI: A novel parallel simulation tool for flapping insect flight using a Fourier method with volume penalization. *SIAM J. Sci. Comput.*, 38(5):S3–S24, 2016.
- [21] A. R. Ennos. Inertial and aerodynamic torques on the wings of diptera in flight. *J. Exp. Biol.*, 142:87–95, 1989.
- [22] I. Faruque and J. S. Humbert. Dipteran insect flight dynamics. part 2: Lateral–directional motion about hover. *J. theor. Biol.*, 265:306–313, 2010.
- [23] J. Finnigan. Turbulence in plant canopies. *Annu. Rev. Fluid Mech.*, 32(1):519–571, 2000.
- [24] S. N. Fry, R. Sayaman, and M. H. Dickinson. The aerodynamics of free-flight maneuvers in Drosophila. *Science (New York, N.Y.)*, 300(5618):495–8, April 2003.
- [25] T. L. Hedrick. Damping in flapping flight and its implications for manoeuvring, scaling and evolution. *J. Exp. Biol.*, 214:4073–4081, 2011.
- [26] T. L. Hedrick, B. Cheng, and X. Deng. Wingbeat time and the scaling of passive rotational damping in flapping flight. *Science*, 324(5924):252–255, 2009.
- [27] T. L. Hedrick and T. L. Daniel. Flight control in the hawkmoth *Manduca sexta*: the inverse problem of hovering. *J. Exp. Biol.*, (209):3114–3130, 2006.

- [28] K. Hirohashi and T. Inamuro. Hovering and targeting flight simulations of a dragonfly-like flapping wing-body model by the immersed boundary-lattice Boltzmann method. *Fluid Dyn. Res.*, 49(4):045502, 2017.
- [29] J. C. R. Hunt, A. A. Wray, and P. Moin. Eddies, stream, and convergence zones in turbulent flows. *Center For Turbulence Research*, pages Report CTR-S88, 1988.
- [30] T. Ishihara and Y. Kaneda. High resolution dns of incompressible homogeneous forced turbulence—time dependence of the statistics—. In *Statistical Theories and Computational Approaches to Turbulence*, pages 177–188. Springer, 2003.
- [31] J. Jiménez, A. A. Wray, P. G. Saffman, and R. S. Rogallo. The structure of intense vorticity in isotropic turbulence. *J. Fluid Mech.*, 255:65–90, 1993.
- [32] J. Kim, D. Kim, and H. Choi. An immersed-boundary finite-volume method for simulations of flow in complex geometries. *Journal of Computational Physics*, 171(1):132 – 150, 2001.
- [33] D. Kolomenskiy, Y. Elimelech, and K. Schneider. Leading-edge vortex shedding from rotating wings. *Fluid Dyn. Res.*, 46:031421, 2014.
- [34] F. O. Lehmann, S. Gorb, N. Nasir, and P. Schützner. Elastic deformation and energy loss of flapping fly wings. *J. Exp. Biol.*, 214:2949–2961, 2011.
- [35] H. Liu. Integrated modeling of insect flight: From morphology, kinematics to aerodynamics. *J. Comput. Phys.*, 228:439–459, 2009.
- [36] H. Liu and K. Kawachi. A numerical study of insect flight. *J. Comput. Phys.*, 146:124–156, 1998.
- [37] H. Liu, D. Kolomenskiy, T. Nakata, and G. Li. Unsteady bio-fluid dynamics in flying and swimming. *Acta Mechanica Sinica*, 33(4):663–684, Aug 2017.
- [38] A. Medina, J. D. Eldredge, J. Kweon, and H. Choi. Illustration of wing deformation effects in three-dimensional flapping flight. *AIAA Journal*, 53(9):2607–2620, March 2015.
- [39] T. Nakata and H. Liu. Aerodynamic performance of a hovering hawkmoth with flexible wings: a computational approach. *Proceedings of the Royal Society B: Biological Sciences*, 279(1729):722–731, 2012.
- [40] T. Nakata and H. Liu. A fluid-structure interaction model of insect flight with flexible wings. *J. Comput. Phys.*, 231(4):1822–1847, 2012.
- [41] R. Noda, T. Nakata, and H. Liu. Body flexion effect on the flight dynamics of a hovering hawkmoth. *J. Biomech. Sc. Engin.*, 9(3):14–004009, 2014.
- [42] Available free of charge and without registration on <https://github.com/pseudospectators/FLUSI>.
- [43] V. M. Ortega-Jimenez, J. S. M. Greeter, R. Mittal, and T. L. Hedrick. Hawkmoth flight stability in turbulent vortex streets. *J. Exp. Biol.*, 216:4567–4579, 2013.
- [44] V. M. Ortega-Jimenez, N. Sapir, M. Wolf, E. A. Variano, and R. Dudley. Into turbulent air: size-dependent effects of von Kármán vortex streets on hummingbird flight kinematics and energetics. *Proc. Biol. Sci.*, 281(1783):20140180, 2014.
- [45] D. Pekurovsky. P3DFFT: a framework for parallel computations of Fourier transforms in three dimensions. *SIAM J. Sci. Comput.*, 34:C192–C209, 2012.
- [46] R. Peyret. *Spectral Methods for Incompressible Viscous Flow*. Springer Berlin / Heidelberg, 2002.
- [47] S. B. Pope. Turbulent flows, 2001.
- [48] M. R. Raupach. Canopy transport processes. In W. L. Steffen and O. T. Denmead, editors, *Flow and Transport in the Natural Environment: Advances and Applications*, pages 95–127, Berlin, Heidelberg, 1988. Springer Berlin Heidelberg.
- [49] M R Raupach and A S Thom. Turbulence in and above plant canopies. *Annu. Ref. Fluid Mech*, 13(1):97–129, 1981.
- [50] S. Ravi, J.D. Crall, A. Fisher, and S. A. Combes. Rolling with the flow: bumblebees flying in unsteady wakes. *J. Exp. Biol.*, 216:4299–4309, 2013.
- [51] S. Ravi, D. Kolomenskiy, T. Engels, K. Schneider, C. Wang, J. Sesterhenn, and H. Liu. Bumblebee minimize control challenges by combining active and passive modes in unsteady winds. *Sci. Rep.*, (6):35043, 2016.
- [52] R. S. Rogallo. Numerical experiments in homogeneous turbulence. *NASA Technical Memorandum*, 81315:1–93, 1981.
- [53] G. Rüppell. Kinematic analysis of symmetrical flight manoeuvres of odonata. *J. Exp. Biol.*, 144:13–42, 1989.
- [54] R. B. Srygley and A. L. R. Thomas. Unconventional lift-generating mechanisms in free-flying butterflies. *Nature*, 420:660–664, 2002.
- [55] M. Sun and J. Tang. Unsteady aerodynamic force generation by a model fruit fly wing in flapping motion. *J. Exp. Biol.*, 205(1):55–70, 2002.
- [56] K. Suzuki and T. Inamuro. Effect of internal mass in the simulation of a moving body by the immersed boundary method. *Computers & Fluids*, 49(1):173 – 187, 2011.
- [57] J. Tukey. *Exploratory Data Analysis*. Addison-Wesley, 1977.
- [58] J. T. Vance, I. Faruque, and J. S. Humbert. Kinematic strategies for mitigating gust perturbations in insects. *Bioinspir. Biomim.*, 8(1):016004, 2013.
- [59] J. C. Wyngaard. Atmospheric turbulence. *Annual Review of Fluid Mechanics*, 24(1):205–234, 1992.
- [60] J. C. Wyngaard. *Turbulence in the Atmosphere*. Cambridge University Press, 2010.
- [61] N. Yokoyama, K. Senda, M. Iima, and N. Hirai. Aerodynamic forces and vortical structures in flapping butterfly’s forward flight. *Phys. Fluids*, 25:021902, 2013.